# Practical Applications of Quantum Sensing: A Simple Method to Enhance the Sensitivity of Nitrogen-Vacancy-Based Temperature Sensors

E. Moreva,[1] E. Bernardi,[1,*] P. Traina,[1] A. Sosso,[1] S. Ditalia Tchernij,[2,3] J. Forneris,[2,3] F. Picollo,[2,3] G. Brida,[1] Ž. Pastuović,[4] I. P. Degiovanni,[1] P. Olivero,[2,3,1] and M. Genovese[1,3]

[1] *Istituto Nazionale di Ricerca Metrologica, Strada delle cacce 91, Turin, Italy*

[2] *Physics Department and NIS Centre of Excellence, University of Torino, Torino, Italy*

[3] *Istituto Nazionale di Fisica Nucleare (INFN) Sez. Torino, Torino, Italy*

[4] *Centre for Accelerator Science, Australian Nuclear Science and Technology Organisation, New Illawarra Road, Lucas Heights, NSW, 2234, Australia*

(Received 23 December 2019; revised manuscript received 3 March 2020; accepted 21 April 2020; published 22 May 2020)

Nitrogen-vacancy centers in diamond allow measurement of environment properties such as temperature, magnetic and electric fields at the nanoscale level, of utmost relevance for several research fields, ranging from nanotechnologies to biosensing. The working principle is based on the measurement of the resonance frequency shift of a single nitrogen-vacancy center (or an ensemble of them), usually detected by monitoring the center photoluminescence emission intensity. Albeit several schemes have already been proposed, the search for the simplest and most effective one is of key relevance for real applications. Here we present a continuous-wave lock-in-based technique able to reach high sensitivity in temperature measurement at microscale or nanoscale volumes (4.8 mK/Hz$^{1/2}$ in $\mu$m$^3$). Furthermore, the present method has the advantage of being insensitive to environmental magnetic noise that in general introduces a bias in the temperature measurement.

DOI: 10.1103/PhysRevApplied.13.054057

## I. INTRODUCTION

Reliable techniques for high-sensitivity nanoscale sensing, eventually exploiting the peculiar properties of quantum systems [1,2], are of absolute importance for several applications ranging from nanotechnology to biophysics. Among them, of particular interest are the innovative approaches to local temperature sensing. These include scanning probe microscopy [3,4], Raman spectroscopy [5], and fluorescence-based measurements using nanoparticles [6,7] and organic dyes [8]. For example, fluorescent polymers and green fluorescent proteins have recently been used for temperature mapping within a living cell [9]. However, many of the existing methods have drawbacks such as poor temporal and spatial resolution, low signal-to-noise ratio, instability in fluorescence emission, and limited operation time. In this perspective, negatively charged nitrogen-vacancy N-$V$ centers in diamond have attracted increasing attention thanks to their unique sensing capabilities [1,10,11]. Sensing techniques based on N-$V$ centers in diamond can be implemented at room temperature; they are also the only technique suited for operating in extreme-pressure conditions [12]. Furthermore they have already been applied inside living cells [13], a feature that makes them ideal sensors for nanoscale bioapplications. By taking advantage of the biocompatibility [14] or anyway of the absence of substantial effects on cell functionality [15], neuronal cells can be grown directly on diamond surfaces [16] or nanodiamonds can be internalized within the cellular body through endocytosis [15]. Thanks to the small dimensions of nanodiamonds, the mapping of temperature fluctuations up to a sensitivity of 200 mK/Hz$^{1/2}$ and at length scales as small as 200 nm is possible in living cells when being integrated with optical microscopic imaging techniques [17,18]. Thus, among other sensing applications, N-$V$-based thermometry is attracting increasing interest [19–28].

Considering the ground triplet state, the degenerate $m_s = \pm 1$ spin states in the absence of an external magnetic field are separated from the $m_s = 0$ state by the zero-field splitting (ZFS) parameter, $D \sim 2.87$ GHz at room temperature, due to spin-spin interactions in the orbital structures of the N-$V$. The ZFS parameter depends on the lattice spacing, which is strongly influenced by the local temperature. For instance, when the local temperature increases, the distance between the localized spins at the N-$V$ center increases, lowering the spin-spin interaction and reducing $D_{gs}$. The ZFS parameter nonlinearly depends on temperature [20], under ambient conditions the temperature dependence being $c_\tau = dD_{gs}/dT \approx -74$ kHz/K [19].

*e.bernardi@inrim.it

 

For a sensor containing $N$ color centers, the temperature sensitivity is given by $\eta = (1/c_\tau)(\Delta\nu/C\sqrt{I_0}\sqrt{N})$, where $\Delta\nu$ and $C$ are, respectively, the spectral width and the contrast of the spin-resonance dip and $I_0$ is the rate of detected photons. Assuming $\Delta\nu$ of the order of 1 MHz and $C \approx 0.3$, a single N-$V$ can potentially exhibit a sensitivity better than 0.76 K/Hz$^{1/2}$ [29]. This value of sensitivity can be improved to 5 mK/Hz$^{1/2}$ [22] using advanced protocols based on pulsed excitation and control [30,31], e.g. based on Rabi oscillations and Ramsey sequences [22–24], or frequency modulation [26,27]. Furthermore, to perform reliable and high-sensitivity temperature measurement the system requires magnetic insulation (for instance from ambient noise or terrestrial magnetic field fluctuations), since the effects of temperature and magnetic field on the resonant frequencies cannot be easily decoupled [22,27]. This, typically, increases the complexity of the setup.

In this work we present a method for nanothermometry based on N-$V$ centers in diamonds, paving the way to practical measurement at the nanoscale because of its simplicity of implementation. Our proof-of-principle experiment is performed in bulk diamond, but the method can be potentially extended to nanodiamonds with the aid of tracking techniques [13]. Specifically, we exploit a sensing scheme with a transverse magnetic field (TF). This results in the suppression of the splitting due to hyperfine interaction, since in this case the expectation value of the spin is small, reducing the coupling between the external magnetic field and the hyperfine field due to the nitrogen nucleus, as described in the following section. This regime, albeit already reported in the literature [32], is used here in temperature sensing, and it can be advantageous in this application on two grounds (see Fig. 1): (i) the dips of the optically detected magnetic resonance (ODMR) spectrum have higher contrast and narrower spectral width with respect to common cw ODMR spectra, due to the degenerate hyperfine structure, and (ii) the presence of a single peak allows the possibility of probing the points of maximum derivative of the ODMR spectrum in a frequency-modulation scheme. The degeneracy of the hyperfine structure can be clearly observed only if the perpendicular component of the magnetic field, $B_\perp$, is strong enough to separate a pair of symmetric dips on a frequency difference that is larger than the hyperfine splitting [41]. A common technique used to increase the sensitivity of ODMR measurements simultaneously probes all three hyperfine peaks related to one spin orientation (simultaneous hyperfine driving, SHfD) instead of probing just one of them. Typically this method increases the sensitivity by a factor of approximately 2. The SHfD technique will be compared with the TF regime in Sec. IV.

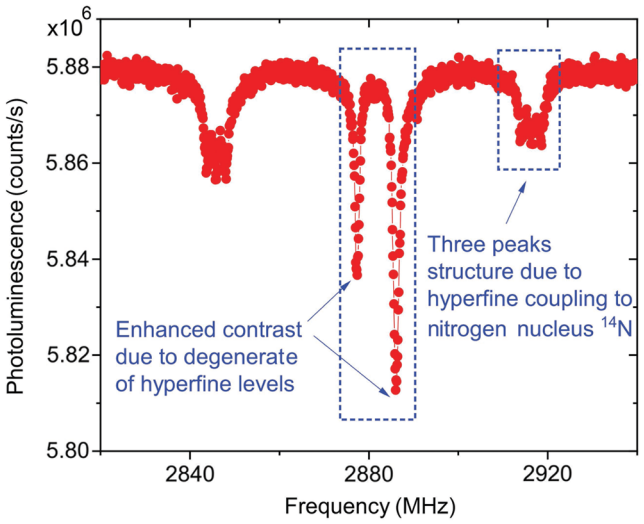


FIG. 1. Optically detected magnetic resonance spectra: orientating the magnetic field **B** orthogonally to the N-$V$ axis suppresses hyperfine contribution resulting in increased contrast and reduced linewidth of the resonant peak and hence in enhanced sensitivity.

## II. DERIVATION OF THE SUPPRESSION OF THE HYPERFINE STRUCTURE DUE TO A TRANSVERSE FIELD

Considering the unperturbed Hamiltonian for a single N-$V$ center:

$$\frac{H_0}{h} = DS_z^2 \tag{1}$$

with the unperturbed eigenvectors and eigenvalues

$$\begin{aligned} |0\rangle &= |S_z = 0\rangle\ 0, \\ |+\rangle &= \frac{1}{\sqrt{2}}(|S_z = +1\rangle + |S_z = -1\rangle)\ D, \\ |-\rangle &= \frac{1}{\sqrt{2}}(|S_z = +1\rangle - |S_z = -1\rangle)\ D, \end{aligned} \tag{2}$$

the effect of an orthogonal magnetic field, which we take aligned along $x$ without any loss of generality assuming an isotropic system in the $x$-$y$ plane, is described by the Hamiltonian

$$\frac{H_\perp}{h} = \frac{g\mu_B}{h}B_x S_x, \tag{3}$$

and the matrix of the complete Hamiltonian in the basis of unperturbed eigenvalues, see Eq. (2), will be

$$\begin{pmatrix} 0 & 0 & \frac{g\mu_B}{h}B_x \\ 0 & D & 0 \\ \frac{g\mu_B}{h}B_x & 0 & D \end{pmatrix}. \tag{4}$$

If $g\mu_B B_\perp/D \ll 1$ we can apply the second-order perturbation theory for degenerate states. The resulting perturbed

eigenstates and eigenvectors are, respectively,

$$\begin{aligned}\frac{E_1}{h} &= -\frac{g^2\mu_B^2 B_\perp^2}{h^2 D},\\ \frac{E_2}{h} &= D,\\ \frac{E_3}{h} &= D + \frac{g^2\mu_B^2 B_\perp^2}{h^2 D}\end{aligned} \tag{5}$$

and

$$\begin{aligned}|1\rangle &= \frac{1}{\sqrt{1+\frac{g^2\mu_B^2 B_\perp^2}{h^2 D^2}}}\left(|0\rangle - \frac{g\mu_B B_\perp}{hD}|+\rangle\right),\\ |2\rangle &= |-\rangle,\\ |3\rangle &= \frac{1}{\sqrt{1+\frac{g^2\mu_B^2 B_\perp^2}{h^2 D^2}}}\left(\frac{g\mu_B B_\perp}{hD}|0\rangle + |+\rangle\right).\end{aligned} \tag{6}$$

The state $|-\rangle$ remains unperturbed; the states $|S_z = 0\rangle$ and $|+\rangle$ are mixed and repel each other.

From Eq. (5) it follows that the transitions $|1\rangle \rightarrow |2\rangle$ and $|1\rangle \rightarrow |3\rangle$ are both shifted to higher values:

$$\begin{aligned}\frac{\Delta_{|1\rangle\rightarrow|2\rangle}}{h} &= D + \frac{g^2\mu_B^2 B_\perp^2}{h^2 D} = E_2 - E_1,\\ \frac{\Delta_{|1\rangle\rightarrow|3\rangle}}{h} &= D + 2\frac{g^2\mu_B^2 B_\perp^2}{h^2 D} = E_3 - E_1.\end{aligned} \tag{7}$$

It is worth calculating the expectation value of the spin in different directions on the perturbed states (6). For the spin along $x$ we have

$$\begin{aligned}\langle 1|S_x|1\rangle &= -2\frac{g\mu_B B_\perp}{hD}\frac{1}{1+\frac{g^2\mu_B^2 B_\perp^2}{h^2 D^2}},\\ \langle 2|S_x|2\rangle &= \langle -|S_x|-\rangle = 0,\\ \langle 3|S_x|3\rangle &= +2\frac{g\mu_B B_\perp}{hD}\frac{1}{1+\frac{g^2\mu_B^2 B_\perp^2}{h^2 D^2}}.\end{aligned} \tag{8}$$

For the spin along $y$ we have

$$\langle 1|S_y|1\rangle = \langle 2|S_y|2\rangle = \langle 3|S_y|3\rangle = 0. \tag{9}$$

For the spin along $z$ we have

$$\langle 1|S_z|1\rangle = \langle 2|S_z|2\rangle = \langle 3|S_z|3\rangle = 0. \tag{10}$$

From these equations it results that the expectation value of the spin is null along the directions orthogonal to the applied field and small along the direction parallel to the applied field.

This implies also that the magnetic moment and hence the coupling with the external magnetic field and hyperfine field due to the nitrogen nucleus are small. Formally, the $^{14}$N nuclear contribution can be expressed as

$$\mathcal{H}_{\text{nucl}} = QI_z^2 + S_z A_\parallel I_z + S_x A_\perp I_x + S_y A_\perp I_y, \tag{11}$$

where $Q$ is quadrupole coupling and $A_\parallel, A_\perp$ are the parallel and normal hyperfine couplings.

We will consider the case of $B_\perp$ along $x$ and calculate the contribution of the nuclear terms to perturbed eigenstates (6) as the expectation value of (11) on these states.

It can be shown that the quadrupolar contribution acts only on nuclear degrees of freedom creating a gap between states with $I_z = 0$ and states with $I_z \pm 1$.

Considering the hyperfine term for the $|I_z = +1\rangle|3\rangle$ state:

$$\begin{aligned}&\langle 3|\langle I_z = +1|\mathcal{H}_{\text{hyper}}|I_z = +1\rangle|3\rangle\\ &\quad= \langle 3|\langle I_z = +1|S_z A_\parallel I_z + S_x A_\perp I_x + S_y A_\perp I_y|I_z = +1\rangle|3\rangle\\ &\quad= \langle 3|\langle I_z = +1|S_z A_\parallel I_z|I_z = +1\rangle|3\rangle\\ &\qquad+ \langle 3|\langle I_z = +1|S_x A_\perp I_x|I_z = +1\rangle|3\rangle\\ &\qquad+ \langle 3|\langle I_z = +1|S_y A_\perp I_y|I_z = +1\rangle|3\rangle\\ &\quad= A_\parallel\langle 3|S_z|3\rangle\langle I_z = +1|I_z|I_z = +1\rangle\\ &\qquad+ A_\perp\langle 3|S_x|3\rangle\langle I_z = +1|I_x|I_z = +1\rangle\\ &\qquad+ A_\perp\langle 3|S_y|3\rangle\langle I_z = +1|I_y|I_z = +1\rangle = 0,\end{aligned} \tag{12}$$

because the only non-null term for electronic degrees of freedom is $\langle 3|S_x|3\rangle$, but in this case the nuclear term $\langle I_z = +1|I_x|I_z = +1\rangle$ is null. Similarly

$$\begin{aligned}\langle 3|\langle I_z = 0|\mathcal{H}_{\text{hyper}}|I_z = 0\rangle|3\rangle = 0,\\ \langle 3|\langle I_z = +1|\mathcal{H}_{\text{hyper}}|I_z = +1\rangle|3\rangle = 0.\end{aligned} \tag{13}$$

Along the same lines it can be shown that

$$\begin{aligned}\langle 2|\langle I_z = 0|\mathcal{H}_{\text{hyper}}|I_z = 0\rangle|2\rangle = 0,\\ \langle 2|\langle I_z = +1|\mathcal{H}_{\text{hyper}}|I_z = +1\rangle|2\rangle = 0,\\ \langle 2|\langle I_z = -1|\mathcal{H}_{\text{hyper}}|I_z = -1\rangle|2\rangle = 0,\end{aligned} \tag{14}$$

and

$$\begin{aligned}\langle 1|\langle I_z = 0|\mathcal{H}_{\text{hyper}}|I_z = 0\rangle|1\rangle = 0,\\ \langle 1|\langle I_z = +1|\mathcal{H}_{\text{hyper}}|I_z = +1\rangle|1\rangle = 0,\\ \langle 1|\langle I_z = -1|\mathcal{H}_{\text{hyper}}|I_z = -1\rangle|1\rangle = 0.\end{aligned} \tag{15}$$

Concluding, the quadrupole interaction aligns nuclear spin along the N-$V$ axis but perturbed electronic states have a small electronic spin different from zero only in a direction orthogonal to the N-$V$ axis. Thus, for a magnetic field aligned orthogonally to the N-$V$ axis the hyperfine interaction has no effect on the level structure and hence no hyperfine structure is present (see Fig. 2).

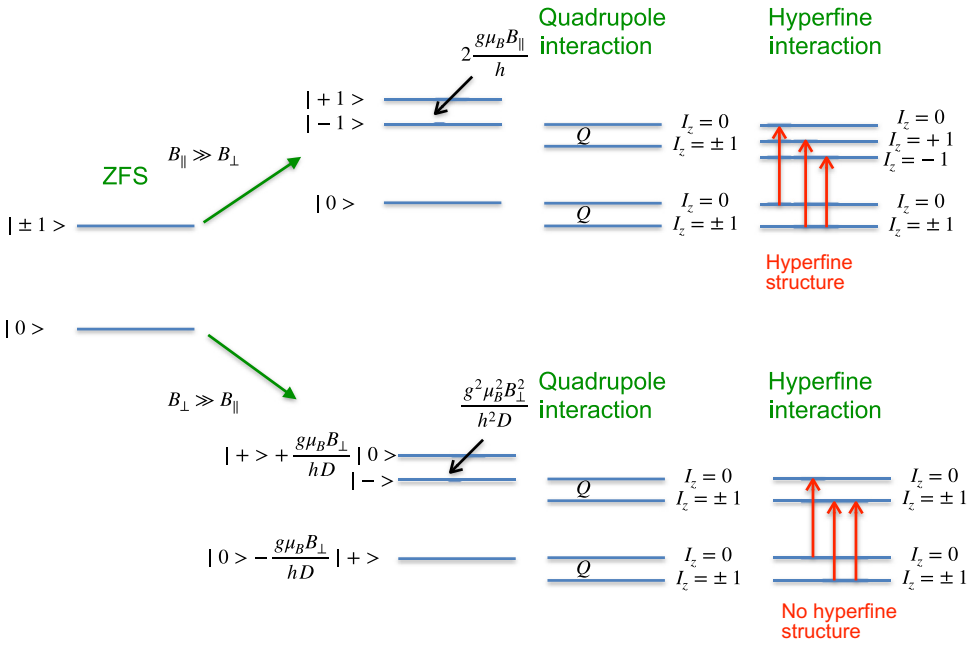


FIG. 2. Energy level diagram for axial and transverse magnetic field.

## III. EXPERIMENTAL METHODS

Our setup (Fig. 3) is based on an inverted microscope (Olympus IX73), adapted to confocal measurements with single-photon sensitivity. The sensor consists of a CVD diamond sample (Element Six) with $3 \times 3 \times 0.3$ mm$^3$ substrate, having $< 1$ and $< 0.05$ ppm concentrations of substitutional nitrogen and boron, respectively. The N-$V$ sensing volume is fabricated via the implantation of 10 keV $^{14}N^+$ ions with a fluence of $10^{14}$ ions cm$^{-2}$ followed by a thermal annealing at 950 °C for 2 h. The process results in the formation of an approximately 10-nm-thick layer of N-$V$ centers with a concentration of $n_{\text{N-}V} \sim 3 \times 10^{19}$ cm$^{-3}$. The diamond sample is mounted on a microwave planar ring antenna, specifically designed for ODMR measurements at frequencies within a 400-MHz range centered around the 2.87-GHz spin resonance [33], in the temperature-controlled chamber (293.15–318.15 K, $\pm$ 0.1 K) of the microscope. As a reference, temperature measurement with a precision of $5 \times 10^{-3}$ K is also carried out, exploiting a thermocouple fixed on the top of the diamond by means of thermoconductive glue.

Excitation light (80 mW optical power) at 532 nm is obtained from the second harmonic of a Nd:YAG laser with high power stability (Coherent Prometheus 100NE) and is focused close to the lower side of the diamond sample through an air objective (Olympus UPLANFL) with NA = 0.67. The photoluminescence (PL), spectrally filtered with notch at 532 nm and long-pass filter at 650 nm, is collected and detected with two different acquisition systems. A 4% fraction of the total PL intensity is sent to a single-photon detector (SPD). The signal from the SPD is used for the ODMR spectrum acquisition. The remaining 96% fraction of the emitted PL intensity is collected by a NA = 0.25 objective (Olympus 10×) and imaged onto a bias photodetector (Thorlabs DET 10A2). An external magnetic field is applied to the diamond sample using a permanent magnet fixed on a translation stage allowing micrometric movement along the three spatial axes. The minimum magnet-sample distance achievable with our apparatus is 4 cm because of the thickness of the chamber. In our case, the magnetic field is approximately 6 mT. This transverse applied field is low and does not suppress the ODMR contrast [34]. In addition, a coil is used for magnetic field modulation.

Microwave control is achieved using a commercial microwave (MW) generator (Keysight N5172B) whose central frequency is internally frequency modulated at

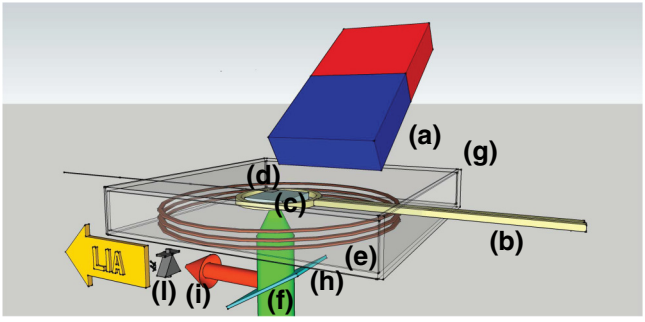


FIG. 3. Schematic of the experimental setup. (a) Permanent magnet. (b) Microwave planar ring antenna. (c) CVD diamond sample. (d) Thermocouple. (e) Coil. (f) Green excitation laser. (g) Temperature-controlled chamber. (i) Red photoluminescence. (l) Photodetector.

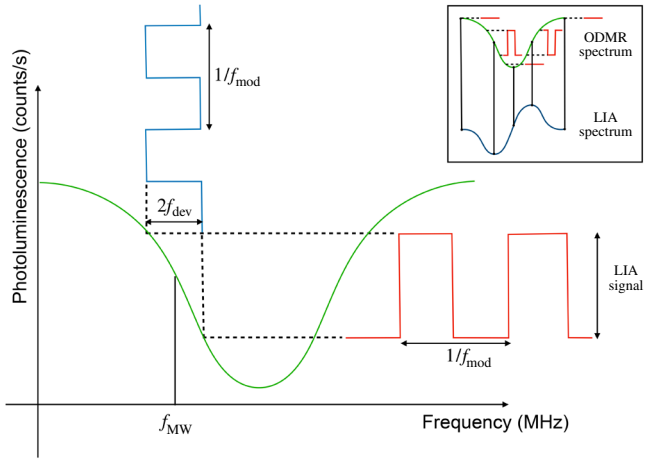


FIG. 4. Schematic of the lock-in amplifier (LIA) technique. The frequency of the microwave excitation $f_{MW}$ is modulated by a wave of amplitude $f_{dev}$ and frequency $f_{mod}$. The resulting modulated photoluminescence signal, modulated at frequency $f_{mod}$, is detected by a LIA. A temperature shift or an applied magnetic field induces a shift in the resonance frequency and hence a variation in the lock-in signal. In the inset is shown how the LIA spectrum derives from the ODMR spectrum. The red lines represent the modulated photoluminescence signal for different $f_{MW}$. The LIA signal is greater at points of maximum derivative of the ODMR signal and it is null at the resonance of the ODMR signal.

$f_{mod} = 1009$ Hz with a modulation depth $f_{dev} = 0.6$ MHz. The output MW signal is amplified and then sent to the microwave antenna. The photodiode is connected to the low-noise current input of a Stanford SR860 lock-in amplifier (LIA) that provides phase-sensitive demodulation of the fluorescence signal (see Fig. 4). In order to operate in the SHfD regime, the MW signal is mixed via a double balanced mixer with an approximately 2.16-MHz sine wave to create two simultaneous driving modulated frequencies near the selected resonance transition.

The measurement requires a preliminary calibration to determine the dependence on temperature of parameter $D$. This calibration is carried out by determining the MW frequency for which the LIA signal is zero for different temperatures measured with the thermocouple. From this calibration a value of $c_\tau = (-76.5 \pm 0.3)$ kHz/K is obtained. The actual temperature measurement is carried out by fixing the MW frequency and recording the variation of the LIA signal with time (averaging time of 1 s, lock-in time constant $\tau = 10$ ms). This is related to the variation in temperature through the slope of the LIA spectrum and the parameter $c_\tau$.

In order to characterize the sensitivity of our temperature measurement method, time traces of the LIA output signal are recorded and a root-mean-square amplitude spectral density is calculated using the Hanning window function. Noise contributions arising from laser, microwave excitation and electronic noise of the lock-in amplifier are accounted for. In addition, cw shot-noise limit is calculated, as described in Appendix B. The MW frequency is tuned to the center of the resonance, where the lock-in signal crosses zero and thus provides the largest temperature response. The low-frequencies plateau of the curves expresses the experimental sensitivity.

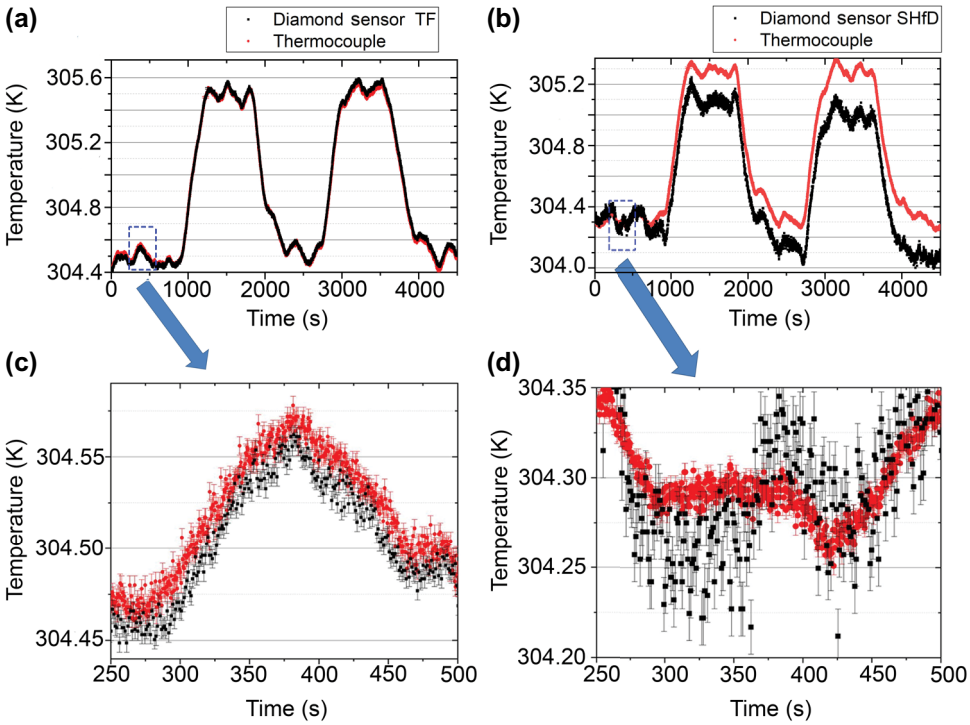


FIG. 5. Response of the N-$V$ sensor (black line) in the proposed regime compared to the readout of a standard thermocouple (red line) to repeated thermal cycles. The period of the repetition is 1800 s and the temperature variation is 1 K. (a),(c) The TF regime, showing almost perfect agreement of the measurement values; (b),(d) SHfD. The lack of agreement between the two traces in the latter case is attributed to environmental field fluctuations. Panels (c),(d) are the enlargements of panels (a),(c), where the enlarged zone is defined by the blue dashed rectangle. The error bars are smaller than the experimental points in (a),(b), but they can be appreciated in (c),(d).

## IV. RESULTS AND DISCUSSION

With the independent calibration of the temperature dependence of $D$, we carry out temperature measurements by exploiting both our technique and the one based on SHfD, as respectively reported in Figs. 5(a) and 5(b). Figure 5(a) shows the response of the N-$V$ sensor (black line) to repeated thermal cycles (period of 1800 s, temperature variation of 1 K) compared to the readout of a standard thermocouple (red line). The results show the excellent agreement between these two measurements performed with independent devices. We point out that the uncertainty of the SHfD method in Fig. 5(c) is about 3 times larger than for the transverse bias regime. Furthermore, we note that in the latter case there is no agreement between the two traces at increasing times. This is due to periodic fluctuations of environmental magnetic field. Instead, in our technique the contribution of the magnetic field appears only at the second order in the Hamiltonian, thus protecting the measurements from fluctuations of environmental magnetic field. In our case, by fitting the curve, a sensitivity value as low $(4.8 \pm 0.4)$ mK/Hz$^{1/2}$ is demonstrated. In Fig. 6, showing the linear spectral density of the sensed signal (acquisition time of 10 min, lock-in time constant $\tau = 1$ ms), we note that the sensitivity obtained with our method (red curves) with respect to the one achieved by SHfD (blue curves) is enhanced by a factor of approximately 3, coherent with the result in Fig. 5. The electronic noise floor is about 2 mK/Hz$^{1/2}$. The other major noise contribution comes from laser fluctuations, with results near to the cw shot-noise limit: thus the "physical" limit to our innovative method is significantly lower. To further demonstrate the resilience of our technique to external magnetic fields, we inject an additional oscillating (25 Hz) magnetic field. The effect of this magnetic field is significantly different for the two techniques, as can be seen in Fig. 6, where the peak in the spectrum corresponding to this magnetic signal is one order of magnitude less prominent with our technique as compared to the SHfD method [42]. This is consistent with the fact that the main harmonics present in the SHfD spectrum substantially disappear, demonstrating that our technique is less sensitive to magnetic noise. In our proof-of-principle measurements we use a bulk diamond, which allows the measurement of the average temperature through the whole sample due to the high thermal conductivity of this material ($\lambda = 2500$ W m$^{-1}$ K$^{-1}$). This is necessary so as to compare our results with the reading of the thermocouple. Practical nanoscale sensing can be realized with this technique using nanodiamond sensors and tracking techniques.

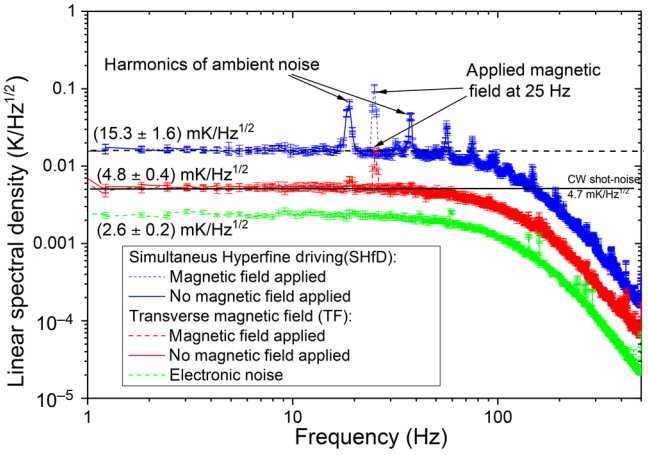


FIG. 6. Comparison between the linear spectral densities of the readout of the N-$V$ sensor in the TF regime (red line) and in the SHfD case (blue line). The dashed (continuous) lines correspond to the application (disabling) of an oscillating (25 Hz) magnetic field to the sample. It is apparent from the continuous lines that an improved sensitivity (lower than 5 mK/Hz$^{1/2}$) is achieved with our method. From the dashed lines it is demonstrated that with our technique the peak due to the 25-Hz magnetic field is one order of magnitude less prominent in our regime, proving the reduced sensitivity to magnetic noise.

## V. CONCLUSIONS

In conclusion, in this article we present a technique for temperature sensing with N-$V$ centers in diamond, allowing the reaching of a high sensitivity without the need of a complex experimental setup, such as for instance the implementation of articulated pulse sequences, while at the same time protecting the measurement from the effect of environmental magnetic noise (which represents one of the most significant limits of currently used techniques). Indeed, our technique only requires the alignment of the bias magnetic field along the orthogonal direction of the N-$V$ axis. In particular we have obtained a noise floor $< 5$ mK/Hz$^{1/2}$, which represents a value comparable with the best results achieved up to now [27] (430 $\mu$K/Hz$^{1/2}$) when the sensitivity is normalized to the sensing volume (approximately 1 $\mu$m$^3$ in our case, approximately $5 \times 10^3$ $\mu$m$^3$ in Ref. [27]). On the other hand, techniques based on ZPL shift [35–40], albeit simpler, are not competitive in terms of sensitivity (usually about 500 mK/Hz$^{1/2}$), eventually reduced to 13 mK/Hz$^{1/2}$ but at the cost of a more complex measurement protocol [37], i.e., a multiparametric analysis of photoluminescence and acquisition time. In a short-time perspective, this technique can be extended to nanoscale or intracellular sensing by using nanodiamonds instead of a bulk crystal. Also, the use of transverse field regime for pulsed sequences, like a Ramsey scheme measurement, is promising, as demonstrated by the fact that in this regime the ODMR remains narrow. A further straightforward extension of the method would be based on the use of the degenerate resonances as a closed-loop control for the other, nondegenerate, resonances allowing for simultaneous, independent monitoring of both the magnetic field and the temperature. Finally,

this method because of its simplicity and high sensitivity could boost developments in the field of quantum-assisted temperature sensing and it has foreseeable applications in high-sensitivity nanoscale thermometry and, thanks to the biocompatibility of diamond, in biosensing.

## ACKNOWLEDGMENTS

This work has received funding from the European Union's PATHOS EU H2020 FET-OPEN Grant No. 828946 and Horizon 2020 and the EMPIR Participating States in the context of the projects EMPIR-17FUN06 "SIQUST" and 17FUN01 BeCOMe, from the project "Piemonte Quantum Enabling Technologies" (PiQuET), funded by the Piemonte Region within the "Infra-P" scheme (POR-FESR 2014-2020 program of the European Union), from Departments of Excellence Project (L. 232/2016), funded by MIUR, from Coordinated Research Project F11020 of the International Atomic Energy Agency (IAEA), and from the Australian Government through the NCRIS programme. The authors acknowledge the technical support received from Elio Bertacco, Vanna Pugliese, Simone D'Agostino, Fabio Bertiglia, and Giuseppina Lo Pardo.

## APPENDIX A: LIA SPECTRA FOR TRANSVERSE FIELD REGIME AND NORMAL REGIME

A further corroboration of the resilience of our technique to external magnetic fields is given in Fig. 7. In this figure, the shift induced in LIA spectra by an additional magnetic field in the TF regime is compared to the one in the standard regime. The additional magnetic field is applied along the (100) direction in order to have the same projection in module for both regimes. It can be noted that the resonance shift in the TF regime is one order of magnitude smaller than the one in the normal regime.

## APPENDIX B: SHOT-NOISE LIMIT CALCULATION

The cw shot-noise limit is

$$\eta_{\mathrm{cw}} = \frac{1}{c_\tau} \frac{\sqrt{I_0}}{\max\left(\frac{\partial I_0}{\partial \nu}\right)}, \tag{B1}$$

where $c_\tau = 74.2$ kHz/K. We can estimate it from data in Fig. 1 of the main text considering the equivalent expression

$$\eta_{\mathrm{cw}} = K \frac{1}{c_\tau} \frac{\Delta\nu}{\sqrt{I_0 C}} = 4.7\ \mathrm{mK/Hz^{1/2}}, \tag{B2}$$

where $\Delta\nu = 1.1$ MHz is the linewidth, $C = 0.64\%$ is the contrast for the left-hand ODMR peak related to the TF regime, see Fig. 1 in the main text, and $K = 0.31$ is our specific linewidth. $I_0 = 3.03 \times 10^{10}\ \mathrm{s^{-1}}$ is estimated from the optical power incident on the photodiode, $W = 8.5$ nW, considering a photon energy $E_{\mathrm{ph}} = 2.84 \times 10^{-19}$ J. It is worth noticing that, using lock-in detection, the points of maximum derivative are probed on both sides of the peak. This implies that the signal increases by a factor of 2 and the noise by a factor of $\sqrt{2}$, leading to a shot-noise limit lowered by a factor of $\sqrt{2}$ for lock-in detection compared to the value expressed in Eq. (A2).

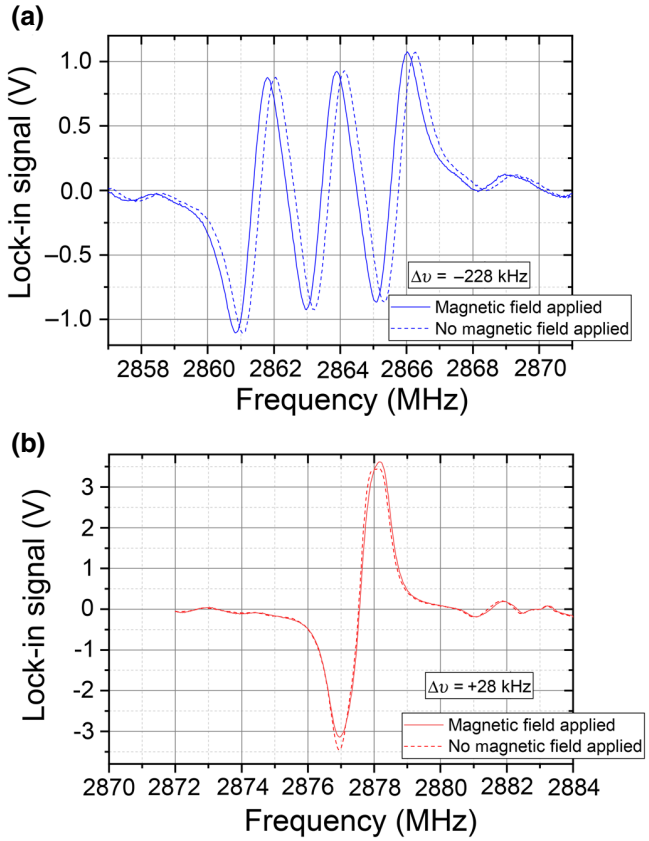


FIG. 7. LIA spectra for standard regime (a) and transverse field regime (b) with and without the application of an additional field ($\approx 1\ \mu$T) along the (100) direction. The lock-in time constant is set to $\tau = 100$ ms.

[1] Christian L. Degen, F. Reinhard, and Paola Cappellaro, Quantum sensing, Rev. Mod. Phys. **89**, 035002 (2017).
[2] Marco Genovese, Real applications of quantum imaging, J. Opt. **18**, 073002 (2016).
[3] Yanan Yue and Xinwei Wang, Nanoscale thermal probing, Nano Rev. **3**, 11586 (2012).
[4] Thomas D. Vreugdenburg, Cameron D. Willis, Linda Mundy, and Janet E. Hiller, A systematic review of elastography, electrical impedance scanning, and digital infrared thermography for breast cancer screening and diagnosis, Breast Cancer Res. Treat. **137**, 665 (2013).

[5] Séverine Gomès, Ali Assy, and Pierre-Olivier Chapuis, Scanning thermal microscopy: A review, Phys. Status Solidi (A) **212**, 477 (2015).
[6] Jui-Ming Yang, Haw Yang, and Liwei Lin, Quantum dot nano thermometers reveal heterogeneous local thermogenesis in living cells, ACS Nano **5**, 5067 (2011).
[7] Soo Ho Kim, Jermim Noh, Min Ku Jeon, Ki Woong Kim, Luke P. Lee, and Seong Ihl Woo, Micro-raman thermometry for measuring the temperature distribution inside the microchannel of a polymerase chain reaction chip, J. Micromech. Microeng. **16**, 526 (2006).
[8] Fiorenzo Vetrone, Rafik Naccache, Alicia Zamarrón, Angeles Juarranz de la Fuente, Francisco Sanz-Rodríguez, Laura Martinez Maestro, Emma Martín Rodriguez, Daniel Jaque, José García Solé, and John A. Capobianco, Temperature sensing using fluorescent nanothermometers, ACS Nano **4**, 3254 (2010).
[9] Zhaoyang Ding, Chunfei Wang, Gang Feng, and Xuanjun Zhang, Thermo-responsive fluorescent polymers with diverse lcsts for ratiometric temperature sensing through fret, Polymers **10**, 283 (2018).
[10] Gopalakrishnan Balasubramanian, Andrii Lazariev, Sri Ranjini Arumugam, and De-wen Duan, Nitrogen-vacancy color center in diamond-emerging nanoscale applications in bioimaging and biosensing, Curr. Opin. Chem. Biol. **20**, 69 (2014).
[11] Jacopo Forneris, S. Ditalia Tchernij, Paolo Traina, Ekaterina Moreva, Natko Skukan, Milko Jakšić, Veljko Grilj, Federico Bosia, Emanuele Enrico, and Giampietro Amato *et al.*, Mapping the Local Spatial Charge in Defective Diamond by Means of n-V Sensors? A Self-Diagnostic Concept, Phys. Rev. Appl. **10**, 014024 (2018).
[12] James J. Hamlin and Brian B. Zhou, Extreme diamond-based quantum sensors, Science **366**, 1312 (2019).
[13] Liam P. McGuinness, Yuling Yan, Alastair Stacey, David A. Simpson, Liam T. Hall, Dougal Maclaurin, Steven Prawer, P. Mulvaney, J. Wrachtrup, and F. Caruso *et al.*, Quantum measurement and orientation tracking of fluorescent nanodiamonds inside living cells, Nat. Nanotechnol. **6**, 358 (2011).
[14] Shu-Jung Yu, Ming-Wei Kang, Huan-Cheng Chang, Kuan-Ming Chen, and Yueh-Chung Yu, Bright fluorescent nanodiamonds: No photobleaching and low cytotoxicity, J. Am. Chem. Soc. **127**, 17604 (2005).
[15] Laura Guarina, C. Calorio, D. Gavello, E. Moreva, P. Traina, A. Battiato, S. Ditalia Tchernij, J. Forneris, M. Gai, F. Picollo *et al.*, Nanodiamonds-induced effects on neuronal firing of mouse hippocampal microcircuits, Sci. Rep. **8**, 1 (2018).
[16] Christian G. Specht, Oliver A. Williams, Richard B. Jackman, and Ralf Schoepfer, Ordered growth of neurons on diamond, Biomaterials **25**, 4073 (2004).
[17] Georg Kucsko, Peter C. Maurer, Norman Ying Yao, Michael Kubo, Hyun Jong Noh, Po Kam Lo, Hongkun Park, and Mikhail D. Lukin, Nanometre-scale thermometry in a living cell, Nature **500**, 54 (2013).
[18] D. Gatto Monticone, K. Katamadze, Paolo Traina, E. Moreva, Jacopo Forneris, Ivano Ruo-Berchera, Paolo Olivero, I. P. Degiovanni, Giorgio Brida, and M. Genovese, Beating the Abbe Diffraction Limit in Confocal Microscopy via Nonclassical Photon Statistics, Phys. Rev. Lett. **113**, 143602 (2014).
[19] Victor M. Acosta, Erik Bauch, Micah P. Ledbetter, Amir Waxman, L.-S. Bouchard, and Dmitry Budker, Temperature Dependence of the Nitrogen-Vacancy Magnetic Resonance in Diamond, Phys. Rev. Lett. **104**, 070801 (2010).
[20] X.-D. Chen, C.-H. Dong, F.-W. Sun, C.-L. Zou, J.-M. Cui, Z.-F. Han, and G.-C. Guo, Temperature dependent energy level shifts of nitrogen-vacancy centers in diamond, Appl. Phys. Lett. **99**, 161903 (2011).
[21] Marcus W. Doherty, Victor M. Acosta, Andrey Jarmola, Michael S. J. Barson, Neil B. Manson, Dmitry Budker, and Lloyd C. L. Hollenberg, Temperature shifts of the resonances of the nv- center in diamond, Phys. Rev. B. **90**, 041201 (2014).
[22] Philipp Neumann, Ingmar Jakobi, Florian Dolde, Christian Burk, Rolf Reuter, Gerald Waldherr, Jan Honert, Thomas Wolf, Andreas Brunner, Jeong Hyun Shim *et al.*, High-precision nanoscale temperature sensing using single defects in diamond, Nano Lett. **13**, 2738 (2013).
[23] Junfeng Wang, Fupan Feng, Jian Zhang, Jihong Chen, Zhongcheng Zheng, Liping Guo, Wenlong Zhang, Xuerui Song, Guoping Guo, Lele Fan *et al.*, High-sensitivity temperature sensing using an implanted single nitrogen-vacancy center array in diamond, Phys. Rev. B. **91**, 155404 (2015).
[24] David M. Toyli, F. Charles, David J. Christle, Viatcheslav V. Dobrovitski, and David D. Awschalom, Fluorescence thermometry enhanced by the quantum coherence of single spins in diamond, Proc. Natl. Acad. Sci. **110**, 8417 (2013).
[25] Hannah Clevenson, Matthew E. Trusheim, Carson Teale, Tim Schröder, Danielle Braje, and Dirk Englund, Broadband magnetometry and temperature sensing with a light-trapping diamond waveguide, Nat. Phys. **11**, 393 (2015).
[26] Yan-Kai Tzeng, Pei-Chang Tsai, Hsiou-Yuan Liu, Oliver Y. Chen, Hsiang Hsu, Fu-Goul Yee, Ming-Shien Chang, and Huan-Cheng Chang, Time-resolved luminescence nanothermometry with nitrogen-vacancy centers in nanodiamonds, Nano Lett. **15**, 3945 (2015).
[27] Adam M. Wojciechowski, Mürsel Karadas, Christian Osterkamp, Steffen Jankuhn, Jan Meijer, Fedor Jelezko, Alexander Huck, and Ulrik L. Andersen, Precision temperature sensing in the presence of magnetic field noise and vice-versa using nitrogen-vacancy centers in diamond, Appl. Phys. Lett. **113**, 013502 (2018).
[28] Taras Plakhotnik, Marcus W. Doherty, Jared H. Cole, Robert Chapman, and Neil B. Manson, All-optical thermometry and thermal properties of the optically detected spin resonances of the nv–center in nanodiamond, Nano Lett. **14**, 4989 (2014).
[29] A Dréau, M. Lesik, L. Rondin, P. Spinicelli, O. Arcizet, J.-F. Roch, and V. Jacques, Avoiding power broadening in optically detected magnetic resonance of single nv defects for enhanced dc magnetic field sensitivity, Phys. Rev. B **84**, 195204 (2011).
[30] Zhen-Yu Wang, Jacob E. Lang, Simon Schmitt, Johannes Lang, Jorge Casanova, Liam McGuinness, Tania S. Monteiro, Fedor Jelezko, and Martin B. Plenio, Randomization of Pulse Phases for Unambiguous and Robust Quantum Sensing, Phys. Rev. Lett. **122**, 200403 (2019).

[31] Genko T. Genov, Fedor Jelezko, and Alex Retzker, Efficient and robust signal sensing by sequences of adiabatic chirped pulses, arXiv:1910.01253 (2019).

[32] Florian Dolde, Helmut Fedder, Marcus W. Doherty, Tobias Nöbauer, Florian Rempp, Gopalakrishnan Balasubramanian, Thomas Wolf, Friedemann Reinhard, Lloyd C. L. Hollenberg, Fedor Jelezko *et al.*, Electric-field sensing using single diamond spins, Nat. Phys. **7**, 459 (2011).

[33] Kento Sasaki, Yasuaki Monnai, Soya Saijo, Ryushiro Fujita, Hideyuki Watanabe, Junko Ishi-Hayase, Kohei M. Itoh, and Eisuke Abe, Broadband, large-area microwave antenna for optically detected magnetic resonance of nitrogen-vacancy centers in diamond, Rev. Sci. Instrum. **87**, 053904 (2016).

[34] J. P. Tetienne, L. Rondin, P. Spinicelli, M. Chipaux, T. Debuisschert, J. F. Roch, and V. Jacques, Magnetic-field-dependent photodynamics of single nv defects in diamond: An application to qualitative all-optical magnetic imaging, New J. Phys. **14**, 103033 (2012).

[35] Jing-Wei Fan, Ivan Cojocaru, Joe Becker, Ilya V. Fedotov, Masfer Hassan A. Alkahtani, Abdulrahman Alajlan, Sean Blakley, Mohammadreza Rezaee, Anna Lyamkina, Yuri N. Palyanov *et al.*, Germanium-vacancy color center in diamond as a temperature sensor, ACS Photonics **5**, 765 (2018).

[36] Masfer Alkahtani, Ivan Cojocaru, Xiaohan Liu, Tobias Herzig, Jan Meijer, Johannes Küpper, Tobias Lühmann, Alexey V. Akimov, and Philip R. Hemmer, Tin-vacancy in diamonds for luminescent thermometry, Appl. Phys. Lett. **112**, 241902 (2018).

[37] Sumin Choi, Viatcheslav N. Agafonov, Valery A. Davydov, and Taras Plakhotnik, Ultrasensitive all-optical thermometry using nanodiamonds with a high concentration of silicon-vacancy centers and multiparametric data analysis, ACS Photonics **6**, 1387 (2019).

[38] Christian T. Nguyen, Ruffin E. Evans, Alp Sipahigil, Mihir K. Bhaskar, Denis D. Sukachev, Viatcheslav N. Agafonov, Valery A. Davydov, Liudmila F. Kulikova, Fedor Jelezko, and Mikhail D. Lukin, All-optical nanoscale thermometry with silicon-vacancy centers in diamond, Appl. Phys. Lett. **112**, 203102 (2018).

[39] Toan Trong Tran, Blake Regan, Evgeny A. Ekimov, Zhao Mu Yu Zhou, Wei-bo Gao, Prineha Narang, Alexander S. Solntsev, Milos Toth, Igor Aharonovich *et al.*, Anti-stokes excitation of solid-state quantum emitters for nanoscale thermometry, Sci. Adv. **5**, eaav9180 (2019).

[40] Mingyang Yang, Qilong Yuan, Jingyao Gao, Shengcheng Shu, Feiyue Chen, Huifang Sun, Kazuhito Nishimura, Shaolong Wang, Jian Yi, Cheng-Te Lin *et al.*, A diamond temperature sensor based on the energy level shift of nitrogen-vacancy color centers, Nanomaterials **9**, 1576 (2019).

[41] This corresponds to $B_\perp = (h/g\mu_B)\sqrt{A_\parallel D_{gs}}$, where $A_\parallel = 2.16$ MHz is the parallel hyperfine interaction with the $^{14}$N nuclear spin, $g$ is the Landé factor, and $\mu_B$ is the Bohr magneton. Thereby the boundary condition is $B_\perp > 2.8$ mT. In our case the contribution from nonaxial strain is negligible.

[42] The oscillating magnetic field ($\approx 100$ nT) is applied along the (100) direction, resulting in projection of equal magnitude along every N-$V$-axis orientation.